ADVANCED FUNCTIONAL MATERIALS

Exact Scaling Laws for Electrical Conductivity Properties of Nematic Polymer Nanocomposite Monodomains**

By *Xiaoyu Zheng*, *M. Gregory Forest*,* *Robert Lipton*, *Ruhai Zhou*, and *Qi Wang*

The purpose of this paper is to connect two critical aspects of nanocomposite materials engineering: the knowledge of the orientational distribution of quiescent or flowing anisotropic macromolecules, and homogenization theory of composites with spheroidal inclusions at low volume fractions. The nano-elements considered herein are derived from the class of high-aspect-ratio nematic polymers, either rod-like or platelet spheroids. By combining the two features, we derive the *effective electrical conductivity tensor* in closed form. Scaling properties of enhanced conductivity versus volume fraction and weak shear rate become explicit. The most dramatic effect is that the effective conductivity tensor inherits hysteresis, bi-stability, and discontinuous jumps from the isotropic–nematic first-order phase transition. These formulas reveal finer estimates that depend on a competition between two inherently extreme parameters in nematic polymer nanocomposites: the molecular aspect ratio and the conductivity ratio of the inclusions and matrix. Herein, we confine our attention to steady monodomain orientational distributions at rest and in weak shear flows, which serve as benchmarks and guides for future extensions and numerical approaches.

1. Introduction

Nano-elements with high-contrast properties are combined at low (0.1–5 %) volume fractions with traditional polymeric materials to enhance a diverse set of targeted properties.[1] Notable examples are the high electrical conductivity and strength of carbon nanotubes (CNTs) and the barrier properties of nanoclay platelets. Current numerical algorithms for composite properties[2] impose either a random distribution or perfect alignment of the nanorods or nanoplatelets. These opposite extremes of orientational probability distribution functions (PDFs) are assumed not because of the inability to handle real molecular distributions, but, rather, because of a lack of experimental data or model simulations. Indeed, it is a monumental challenge to infer molecular orientational distributions from experimental methods, although important features of the second moment of the PDF are routinely measured with light-scattering methods.[3] Our goal here is to use kinetic and mesoscopic models to generate the PDF or its moments, which can then be linked to composite property theory and numerical algorithms. This strategy becomes more compelling when the kinetic theory of Doi and Hess[4–7] or mesoscopic models are separately benchmarked with experimental data on the flow-induced liquid phase of the composite. Herein, we assume a rapid quench from the liquid to solid phase, which maintains the orientational distribution of the nano-inclusions. We also suppress the effects of the inclusion–matrix interphase. The current predictions, when compared with laboratory measurements, provide an estimate of interphase contributions to effective conductivity based on volume-averaged effects. The separate, though related, effects—due to percolation of the nano-elements—are not captured by volume averaging. Strong disparities between the present predictions and experiments would suggest a dominant influence of percolation relative to volume averaging.

The composite properties, no matter whether they are electrical conductivity (the example chosen here), thermal conductivity, gas or liquid permeabilities, or elastic moduli, require an appropriate average, for example, over the nano-element electrical conductivity σ_{nano} with volume fraction θ_2 and the polymer conductivity σ_{poly} with volume fraction $(1-\theta_2)$. The typically strong contrast $\sigma_{\text{nano}}/\sigma_{\text{poly}} \gg 1$ (or $\sigma_{\text{nano}}/\sigma_{\text{poly}} \ll 1$ which arise for thermal insulating composites) by itself is not sufficient to achieve the enhancement; a high degree of anisotropy of the nano-inclusion is equally critical. This enabling geometric effect comes at a price, however, introducing complexity into the orientational molecular distribution at rest and in processing flows.

High-aspect-ratio molecular inclusions are naturally isotropic (randomly oriented) below a critical volume fraction, θ_2^*, but then spontaneously order above θ_2^*, the isotropic–nematic (I–N) phase transition. Only as $\theta_2 \to 1$ is perfect alignment achieved: a limit that is never approached in nanocomposites. The equilibrium orientational distribution function versus θ_2 is

[*] Prof. M. G. Forest, X. Zheng
Department of Mathematics, University of North Carolina–Chapel Hill
Chapel Hill, NC 27599–3250 (USA)
Email: forest@amath.unc.edu
Prof. R. Lipton
Department of Mathematics, Louisiana State University
Baton Rouge, LA 70803–4918 (USA)
Dr. R. Zhou
Department of Mathematics and Statistics, Old Dominion University
Norfolk, VA 23529 (USA)
Prof. Q. Wang
Department of Mathematics, Florida State University
Tallahassee, FL 32306–4510 (USA)

[**] The authors thank Dr. Richard Vaia, Materials Division at Wright Patterson Air Force Base, for valuable advice and suggestions in developing this research topic. This effort was sponsored by the Air Force Office of Scientific Research, Air Force Materials Command, USAF, under grants F49620-02-1-0041 and F49620-02-1-0086, and the National Science Foundation through grants DMS-0204243, 0296064, and 0308019. This work was supported in part by NASA University Research, Engineering and Technology Institute on Bio Inspired Materials (BIMat) under award no. NCC-1-02037.

 DOI: 10.1002/adfm.200400200

numerically available from Doi–Hess kinetic theory with an excluded-volume intermolecular potential, for example, of Onsager or Maier–Saupe type.[8–10] Herein, our goal is to derive exact formulas for the effective electrical conductivity tensor, at rest and in weak shear flows. This choice is made for two purposes: i) to illustrate the approach for exactly solvable conditions where the methodology and results become transparent; and ii) to determine exact scaling properties of the effective conductivity tensor versus molecular and flow parameters, albeit in special limits or with mesoscopic closure approximations.

First, we implement tensor formulas for the kinetic PDF at dilute concentrations, or the second moment of the PDF derived from mesoscopic models at ordered (nematic) concentrations, and substitute these into the low-volume-fraction expansion of the effective electrical conductivity tensor. We calculate the *effective electrical conductivity tensor*, Σ^e, versus volume fraction θ_2, allowing a property comparison of the quiescent isotropic and nematic phases.

Second, nanocomposites are flow-processed, which deforms the distribution at all concentrations θ_2. We use our recent analytical formulas for monodomain, shear-induced PDFs at dilute concentrations,[9] and for second moments of the PDF at nematic concentrations,[11] in the weak shear limit. From these explicit formulas, we quantify the anisotropy and principal values of Σ^e, and thereby predict nanocomposite conductivity enhancement versus concentration at rest and in weak shear flow.

There are two important properties of the molecular orientation distribution function $f(\mathbf{m})$ that are central to materials, whether the processed geometry is that of fibers, films, or molded parts. First is the local orientation distribution of bulk regions called monodomains, which are micrometer-scale mesophases of the spheroidal molecules in viscous solvents. A general characterization of the orientation distribution $f(\mathbf{m})$ for monodomains, versus geometry and concentration of the nano-inclusions, flow type, and flow rate, has only recently come into focus.[8,10,12–15] Second is the heterogeneity of actual materials, consisting of a statistical distribution of local monodomains intertwined with boundary layers called defects and modulational variations in $f(\mathbf{m})$ on longer length scales. These structures remain largely uncharacterized,[16] and their effects on non-uniform properties will be deferred for now. Instead, we focus on the effective properties of monodomains at rest and in weak shear flow.

2. Formulation of the Nanocomposite Effective Conductivity Problem

Consider conduction in three-dimensional media, governed by the constitutive equations, Equations 1a–c

$$\vec{J}(x) = \sum(x)\vec{E}(x) \tag{1a}$$

$$\nabla \cdot \vec{J} = 0 \tag{1b}$$

$$\nabla \times \vec{E} = 0 \tag{1c}$$

where $\vec{J}(x)$ is the current field, $\vec{E}(x) = \nabla\phi$ is the electric field, $-\phi$ is the electric potential, and $\sum(x)$ is the conductivity tensor of the medium. The **effective conductivity** Σ^e provides the constitutive relation between the average current $\langle\vec{J}\rangle$ and average electric field $\langle\vec{E}\rangle$, that is, Equation 2.

$$\langle\vec{J}\rangle = \sum{}^e\langle\vec{E}\rangle \tag{2}$$

Here $\langle\vec{J}\rangle$ and $\langle\vec{E}\rangle$ are the volume average of the current and electric field over the polymer suspension. There are two inherent difficulties in Σ^e: anisotropy due to orientational molecular ordering, and spatial heterogeneity due to length-scale distortions in the orientational distribution. Herein, we characterize the anisotropy of Σ^e for monodomains of nematic polymer nanocomposites (PNCs), but our framework applies to heterogeneous composites.

2.1. Nanocomposite Microstructure

We consider uniform suspensions of ellipsoidal molecular inclusions with electrical conductivity σ_2 and volume fraction θ_2 in a matrix of electrical conductivity σ_1. Later, we restrict our attention to spheroids, the axi-symmetric case, which is the only class of molecules for which Doi–Hess-type hydrodynamic theory is available.

All ellipsoids are assumed to have the same geometry: a, b, c are the three semi-axes, with $a > b = c$ for spheroidal rods and $a = b > c$ for spheroidal platelets. They orient due to excluded-volume interactions and flow according to a probability distribution that is the central object of the Doi–Hess kinetic theory. The theory incorporates the aspect ratio $r = a/b \gg 1$ (rods); $r = c/a \ll 1$ (platelets) in the combination $(r^2-1)/(r^2+1)$.

2.2. The Effective Conductivity Tensor $\Sigma^e_{\theta_2}$

The effective conductivity tensor $\Sigma^e_{\theta_2}$, where we attach the nano-inclusion volume fraction as a subscript, can be computed by a Taylor expansion in the low volume-fraction limit, $\theta_2 \ll 1$, Equation 3[17]

$$\sum{}^e_{\theta_2} = \sigma_1\mathbf{I} + \theta_2(\sigma_2 - \sigma_1)\mathbf{P} + O(\theta_2^2) \tag{3}$$

where $\mathbf{P}$, the orientation-averaged polarization tensor, is given by Equation 4, $\mathbf{E}(\mathbf{m})$ is the polarization tensor, defined below, and $f(\mathbf{m})$ is the orientational probability distribution function of the inclusions. $\mathbf{I}$ is the 3 by 3 identity matrix.

$$\mathbf{P} = \int_{S^2} \mathbf{E}(\mathbf{m})f(\mathbf{m})d\mathbf{m} \tag{4}$$

From Equation 3, the key object to quantify is $\mathbf{P}$, which requires knowledge of two ingredients: $\mathbf{E}(\mathbf{m})$ is a geometric tensor specified by the nano-inclusion geometry, whereas $f(\mathbf{m})$ is the fundamental object of the Smoluchowski equation of Doi–Hess kinetic theory for quiescent or flowing nematic polymers.

ADVANCED FUNCTIONAL MATERIALS

The polarization tensor $\mathbf{E}(\mathbf{m})$ can be computed explicitly (Equation 6) from three scalar depolarization factors,[18] L_a, L_b, $L_c \geq 0$, Equations 5a–d

$$L_a = \frac{abc}{2}\int_0^\infty \frac{ds}{(s+a^2)\sqrt{(s+a^2)(s+b^2)(s+c^2)}} \tag{5a}$$

$$L_b = \frac{abc}{2}\int_0^\infty \frac{ds}{(s+b^2)\sqrt{(s+a^2)(s+b^2)(s+c^2)}} \tag{5b}$$

$$L_c = \frac{abc}{2}\int_0^\infty \frac{ds}{(s+c^2)\sqrt{(s+a^2)(s+b^2)(s+c^2)}} \tag{5c}$$

$$L_a + L_b + L_c = 1 \tag{5d}$$

$$\mathbf{E}(\mathbf{m}) = \left[\left(1+\left(\frac{\sigma_2-\sigma_1}{\sigma_1}\right)L_a\right)\mathbf{mm} + \left(1+\left(\frac{\sigma_2-\sigma_1}{\sigma_1}\right)L_b\right)\mathbf{nn} + \left(1+\left(\frac{\sigma_2-\sigma_1}{\sigma_1}\right)L_c\right)\mathbf{kk}\right]^{-1} \tag{6}$$

where $\mathbf{m}$ is the unit vector along the long axis of length a, $\mathbf{n}$ is the unit vector along the axis of length b, and $\mathbf{k}$ is the unit vector along the axis of length c; refer to Figure 1. All that remains is an explicit characterization of $f(\mathbf{m})$ (which we now develop in several limiting cases, where analytical formulas are possible), and then finally an analysis of the integral, Equation 4. In more generality, numerical data for $f(\mathbf{m})$ can be implemented in this framework, which we defer to a sequel.

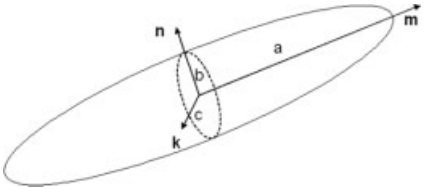

Figure 1. An illustration of spheroidal rods with semi-axes lengths $a > b = c$, with respect to axes $\mathbf{m}$, $\mathbf{n}$, $\mathbf{k}$, respectively.

3. Nanocomposite Properties of Nematic Polymer Monodomains

We proceed to compute the effective conductivity tensor $\Sigma^e_{\theta_2}$ for low-volume-fraction spheroidal suspensions in several limiting regimes:

- The quiescent isotropic phase of dilute random suspensions versus concentration (N) and molecular aspect ratio (r);
- the nematic equilibrium phase versus N and r using second-moment approximate descriptions of the PDF;
- the flow-induced PDF in simple shear at low (isotropic) quiescent concentrations; and
- mesoscopic approximations of the PDF for weak shear-induced nematic phases.

Our first result is to derive an explicit formula for the polarization tensor $\mathbf{P}$, Equation 4, and thereby the effective conductivity tensor $\Sigma^e_{\theta_2}$, Equation 3. This formula is special for spheroidal rod-like (or platelet) nano-inclusions, yet general for any orientational PDF $f(\mathbf{m})$ of the inclusions.

For *rod-like spheroidal nano-inclusions*, the depolarization factors become $L_b = L_c = (1-L_a)/2$ and $\mathbf{mm} + \mathbf{nn} + \mathbf{kk} = \mathbf{I}$, from which we can explicitly express the polarization tensor $\mathbf{E}$ as a linear combination of the isotropic tensor and the quadratic (dyadic) product $\mathbf{mm}$, Equation 7

$$\mathbf{E}(\mathbf{m}) = \left[\left(1+\left(\frac{\sigma_2-\sigma_1}{\sigma_1}\right)L_a\right)\mathbf{mm} + \left(1+\left(\frac{\sigma_2-\sigma_1}{\sigma_1}\right)\frac{1-L_a}{2}\right)(\mathbf{I}-\mathbf{mm})\right]^{-1} \tag{7}$$

We now observe that the inverse of a linear combination of $\mathbf{I}$ and $\mathbf{mm}$ is itself a linear combination of $\mathbf{I}$ and $\mathbf{mm}$. Thus, for spheroids, Equation 7 is explicitly invertible, and we deduce Equation 8

$$\mathbf{E}(\mathbf{m}) = \frac{1}{1+\frac{\sigma_2-\sigma_1}{2\sigma_1}(1-L_a)}\left(\mathbf{I} + \left[\frac{\frac{\sigma_2-\sigma_1}{2\sigma_1}-\frac{3\sigma_2-\sigma_1}{2\sigma_1}L_a}{1+\frac{\sigma_2-\sigma_1}{\sigma_1}L_a}\right]\mathbf{mm}\right) \tag{8}$$

where the spheroidal depolarization factor L_a is explicitly integrable (graphed in Fig. 2), Equation 9

$$L_a = \frac{1-\varepsilon^2}{\varepsilon^2}\left\{\frac{1}{2\varepsilon}\ln\left(\frac{1+\varepsilon}{1-\varepsilon}\right) - 1\right\}, \varepsilon = \sqrt{1-(b/a)^2} \tag{9}$$

The explicit form, Equation 8, of $\mathbf{E}(\mathbf{m})$ has strong consequences. First, even though $f(\mathbf{m})$ generically has an infinite spherical harmonic expansion, by orthogonality relations of spherical harmonics and the linear form, Equation 7, *only the second moments of* $f(\mathbf{m})$ *contribute to* $\mathbf{P}$, Equation 4. This result is valid for any distribution $f(\mathbf{m})$ of monodisperse spheroids, no matter how $f(\mathbf{m})$ is generated, and, furthermore, for both homogeneous monodomains as well as heterogeneous dispersions where $f(\mathbf{m},\mathbf{x})$ varies in space.

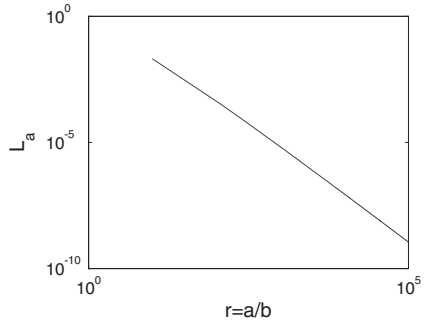

Figure 2. Depolarization factor L_a versus aspect ratio r.

Performing the integral Equation 4 by virtue of Equation 8, we deduce an explicit formula for **P** directly in terms of the second-moment **M**(f) of the orientational probability density f, Equation 10

$$\mathbf{P} = \int_{\|\mathbf{m}\|=1} \mathbf{E}(\mathbf{m}) f(\mathbf{m}) d\mathbf{m} = \frac{1}{1+\frac{\sigma_2-\sigma_1}{2\sigma_1}(1-L_a)} \left(\mathbf{I} + \frac{\frac{\sigma_2-\sigma_1}{2\sigma_1} - \frac{3\sigma_2-\sigma_1}{2\sigma_1} L_a}{1+\frac{\sigma_2-\sigma_1}{\sigma_1} L_a} \mathbf{M} \right) \quad (10)$$

where

$$\mathbf{M} = \mathbf{M}(f) = \langle \mathbf{mm} \rangle = \int_{\|\mathbf{m}\|=1} \mathbf{mm} f(\mathbf{m}) d\,\mathbf{m} \quad (11)$$

Combining Equations 9 and 10 gives the explicit connection between the second moment of the orientational distribution and the overall electrical properties of the nanocomposite, and the central result of this paper:

The effective electrical conductivity tensor $\Sigma^{e}_{\theta_2}$ of the composite is given by Equation 12

$$\Sigma^{e}_{\theta_2} = \Sigma_0 + \sigma_1 \theta_2 (\sigma_2 - \sigma_1) \left(\frac{2}{\sigma_2+\sigma_1-(\sigma_2-\sigma_1)L_a} \mathbf{I} + \frac{(\sigma_2-\sigma_1)(1-3L_a)}{((\sigma_1+\sigma_2)-(\sigma_2-\sigma_1)L_a)(\sigma_1+(\sigma_2-\sigma_1)L_a)} \mathbf{M}(f) \right) + O(\theta_2^2) \quad (12)$$

In general, we define the nanocomposite *electrical conductivity enhancement* in terms of the difference between $\Sigma^{e}_{\theta_2}$ at volume fraction $\theta_2 > 0$ and $\Sigma_0 = \sigma_1 \mathbf{I}$, the isotropic conductivity of the pure matrix with zero volume fraction $\theta_2 = 0$. We shall focus on the principal value(s) of $\Sigma^{e}_{\theta_2}$ and in the generic case of anisotropy, the principal axes of $\Sigma^{e}_{\theta_2}$. The primary formula, Equation 12 already provides intuitively natural results:

The *principal axes of the effective conductivity tensor* $\Sigma^{e}_{\theta_2}$ *are identical to those of* **M**(f(**m**)), which are the so-called "directors" $\mathbf{n}_j$ of the nematic liquid measured in light-scattering experiments. The corresponding order parameter (eigenvalues) d_j of **M**(f), $\mathbf{M}\mathbf{n}_j = d_j \mathbf{n}_j$, which satisfy $0 \le d_j \le 1$, $\sum d_j = 1$, measure the *degrees of optical anisotropy of the composite*. Whenever $d_j \neq 1/3$ or $\mathbf{M} \neq \mathbf{I}/3$, from Equation 12, d_j enter explicitly into the degrees of conductivity anisotropy, which are measured by the eigenvalues σ^{e}_j of Σ^{e}. In a variety of special cases, we will explicitly calculate the distinct principal values (eigenvalues) σ^{e}_j and corresponding principal axes $\mathbf{n}_j$ of $\Sigma^{e}_{\theta_2}$, which then generically lead to *three relative principal value enhancements*, Equation 13

$$\varepsilon_j = \frac{\sigma^{e}_j - \sigma_1}{\sigma_1} = \frac{(\sum^{e}_{\theta_2} - \sum^{e}_{0})}{\sigma_1} : \mathbf{n}_j \mathbf{n}_j, \quad j = 1,2,3 \quad (13)$$

Equivalently, the effective anisotropy tensor $\Sigma^{e}_{\theta_2}$ admits a representation explicitly in terms of its principal axes $\mathbf{n}_j$ and relative enhancements ε_j, Equation 14

$$\sum^{e}_{\theta_2} = \sum_0 + \sigma_1 \sum_{j=1}^{3} \varepsilon_j \mathbf{n}^{t}_j \mathbf{n}_j \quad (14)$$

Equation 12 therefore immediately yields a series of general conclusions, which then form the basis for simplified scaling properties in additional asymptotic limits, either on the molecule geometry or on the contrast between conductivities of the nano-inclusion and matrix.

4. Finer Estimates for High-Contrast Conductivity and Extreme Aspect Ratio

For typical nematic PNCs, two asymptotic limits are routinely observed:

- high-aspect-ratio ($r \gg 1$), spheroidal nano-inclusions, where the molecules depicted in Figure 1 satisfy $a \gg b = c$; then L_a, Equation 9 and Figure 2, admits the asymptotic evaluation, Equation 15

$$L_a = (\log(r)/r^2) + O(r^{-2}) \text{ for } r \gg 1 \quad (15)$$

- high-contrast conductivities, where the nano-inclusion has extreme conductivity σ_2 relative to the matrix value σ_1, Equation 16

$$\sigma_1/\sigma_2 \ll 1 \quad (16)$$

Table 1 indicates typical scaling properties for r, L_a, and σ_1/σ_2 in nematic polymer composites. The fundamental formula, Equation 12, requires a careful analysis of the relative order among these two asymptotic parameters, σ_1/σ_2 and L_a, with the outcome dependent on three possible ranges for the ratio $L_a/(\sigma_1/\sigma_2)$, which we now analyze. These scaling results are valid for any molecular distribution function f(**m**); in the next section, we will assert knowledge of f(**m**) versus nano-element volume fraction and shear rate.

Table 1. Data for the range of typical aspect ratios r and electrical conductivity contrasts σ_1/σ_2 of rod-like nematic polymer nanocomposites.

r	L_a	σ_1/σ_2
$\sim 10^2$–10^5	$\sim 10^{-9}$–10^{-3}	$\sim 10^{-12}$–10^{-5}

Case 1: Suppose $L_a/(\sigma_1/\sigma_2) \gg 1$, e.g., $L_a \sim 10^{-3}$ and $\sigma_1/\sigma_2 \sim 10^{-8}$. Then, the effective conductivity tensor $\Sigma^{e}_{\theta_2}$, Equation 12, and

ADVANCED FUNCTIONAL MATERIALS

corresponding relative enhancement ε_j, Equation 13, have the scaling behavior given by Equation 17

$$\begin{cases} \sum_{\theta_2}^{e} &= \sum_0 + \dfrac{\sigma_1\theta_2}{L_a}\mathbf{M} + O(\theta_2\sigma_1)\mathbf{I} + O(\theta_2\sigma_1)\mathbf{M} + O(\theta_2^2) \\ \varepsilon_j &= \dfrac{\sigma_j^e - \sigma_1}{\sigma_1} = \dfrac{\theta_2}{L_a}d_j + O(\theta_2), \quad j = 1,2,3. \end{cases} \tag{17}$$

Case 2: Suppose $L_a/(\sigma_1/\sigma_2) \sim O(1)$, e.g., $L_a \sim 10^{-6}$ and $\sigma_1/\sigma_2 \sim 10^{-6}$. Then, the scaling properties are given by Equation 18

$$\begin{cases} \sum_{\theta_2}^{e} &= \sum_0 + \dfrac{\theta_2\sigma_2}{1+\frac{L_a}{\sigma_1\sigma_2}}\mathbf{M} + O(\theta_2\sigma_1)\mathbf{I} + O(\theta_2\sigma_1)\mathbf{M} + O(\theta_2^2) \\ \varepsilon_j &= \dfrac{\theta_2(\sigma_2/\sigma_1)}{1+\frac{L_a}{\sigma_1/\sigma_2}}d_j + O(\theta_2), \quad j = 1,2,3 \end{cases} \tag{18}$$

Case 3: Suppose $L_a/(\sigma_1/\sigma_2) \ll 1$, e.g., $L_a \sim 10^{-7}$ and $\sigma_1/\sigma_2 \sim 10^{-5}$. Then, the scaling properties are given by Equation 19

$$\begin{cases} \sum_{\theta_2}^{e} &= \sum_0 + \theta_2\sigma_2\mathbf{M} + O(\theta_2\sigma_1)\mathbf{I} + O(\theta_2\sigma_1)\mathbf{M} + O(\theta_2^2) \\ \varepsilon_j &= \theta_2(\sigma_2/\sigma_1)\,d_j + O(\theta_2), \quad j = 1,2,3 \end{cases} \tag{19}$$

Comments: *The property impact (relative gain) due to the nano-inclusions becomes apparent and significant*. In each case, the relative enhancement of the effective conductivity is captured by a product of the volume fraction $\theta_2 \sim O(10^{-2})$ and either L_a^{-1} or σ_2/σ_1, which are both expected to be comparable to θ_2^{-1} and potentially much greater.

Recall the principal values d_j of $\mathbf{M}(f(\mathbf{m}))$ satisfy $0 \le d_j \le 1$, $\Sigma d_j = 1$. When the distribution is random, all $d_j = 1/3$, and otherwise $1/3 < d_1 < 1$.

So far, these results are quite general; we now inject explicit knowledge about $f(\mathbf{m})$ and $\mathbf{M}(f(\mathbf{m}))$. In the dilute concentration regime, we[9] have recently derived explicit formulas for f in weak shear, and thereby have a precise characterization of $\mathbf{M}(f)$, and consequently $\mathbf{P}$ and $\Sigma^{e}_{\theta_2}$. There are only preliminary analytical characterizations of f at very high nematic concentrations.[19] Nonetheless, decades of mesoscopic theory are based on closing the equations at the second-moment tensor level of resolution of f.[20–22] In particular, we have introduced moment-closure benchmarks based on faithful reproduction of the PDF attractors and phase transitions versus concentration (volume fraction) and shear rate.[11,23] Using special properties of the Doi theory,[11,12] we can easily extend these formulas to any linear planar flow in the weak flow rate limit. In all these cases, we can now give explicit formulas for $\mathbf{P}$ and $\Sigma^{e}_{\theta_2}$. We proceed to several illustrative examples.

5. Applications: Effective Conductivity Tensors for Quiescent and Shear-Induced Mesophases

5.1. Dilute Isotropic Concentrations $f_0(\mathbf{m}) = 1/4\Pi$

If the molecular inclusions are randomly oriented, that is, $f(\mathbf{m}) \equiv 1/(4\pi)$, then $\mathbf{M} = \mathbf{I}/3$ with all $d_j = 1/3$, and the effective conductivity tensor $\Sigma^{e}_{\theta_2}$ remains isotropic (i.e., proportional to $\mathbf{I}$), with an explicit characterization of the inclusions, Equation 20

$$\sum_{\theta_2}^{e} = \sum_0 + \frac{\sigma_1\,\theta_2\,(\sigma_2-\sigma_1)(\sigma_2+5\sigma_1+3(\sigma_2-\sigma_1)L_a)}{3(\sigma_2+\sigma_1-(\sigma_2-\sigma_1)L_a)(\sigma_1+(\sigma_2-\sigma_1)L_a)}\mathbf{I} + O(\theta_2^2) \tag{20}$$

Equivalently, we have the decomposition, Equation 21

$$\sum_{\theta_2}^{e} \approx \sum_0 + \sigma_1\varepsilon^{\mathrm{iso}}\mathbf{I} \tag{21}$$

where the *scalar*, *isotropic*, *relative effective conductivity enhancement* $\varepsilon^{\mathrm{iso}}$ is given by Equation 22

$$\varepsilon^{\mathrm{iso}} = (1/\sigma_1)(\sum_{\theta_2}^{e} - \sum_0^{e}) : \mathbf{nn} = \frac{\theta_2(\sigma_2-\sigma_1)(\sigma_2+5\sigma_1+3(\sigma_2-\sigma_1)L_a)}{3(\sigma_2+\sigma_1-(\sigma_2-\sigma_1)L_a)(\sigma_1+(\sigma_2-\sigma_1)L_a)} + O(\theta_2^2) \tag{22}$$

where $\mathbf{n}$ is any unit vector, since for isotropic tensors, any unit vector is a principal axis.

For high-contrast and high-aspect-ratio molecular elements at dilute concentrations in the isotropic phase, we simply insert into the formulas in Section 4, or analyze Equations 20 or 21 directly, with the following results (Equations 23–25):

- When $L_a/(\sigma_1/\sigma_2) \gg 1$,

$$\begin{cases} \sum_{\theta_2}^{e} &\approx \sigma_1(1 + \dfrac{\theta_2}{3L_a})\mathbf{I} \\ \varepsilon^{\mathrm{iso}} &\approx \dfrac{\theta_2}{3L_a} \end{cases} \tag{23}$$

- When $L_a/(\sigma_1/\sigma_2) \sim O(1)$,

$$\begin{cases} \sum_{\theta_2}^{e} &\approx \sigma_1\left(1 + \dfrac{\theta_2(\sigma_2/\sigma_1)}{3(1+\frac{3L_a}{\sigma_1/\sigma_2})}\right)\mathbf{I} \\ \varepsilon^{\mathrm{iso}} &\approx \dfrac{\theta_2(\sigma_2/\sigma_1)}{3(1+\frac{L_a}{\sigma_1/\sigma_2})} \end{cases} \tag{24}$$

- When $L_a/(\sigma_1/\sigma_2) \ll 1$,

$$\begin{cases} \sum_{\theta_2}^{e} & \approx & \sigma_1(1+\dfrac{\theta_2\sigma_2}{3\sigma_1})\mathbf{I} \\ \varepsilon^{\mathrm{iso}} & \approx & \dfrac{\theta_2(\sigma_2/\sigma_1)}{3} \end{cases} \tag{25}$$

These formulas explicitly clarify that, *even at quiescent dilute concentrations*, when, for example, $\theta_2 \approx 5\times10^{-3}$, *a high conductivity contrast* ($\sigma_1/\sigma_2 \ll 1$) *or an extreme molecular aspect ratio will overwhelm the low volume fraction and conservatively lead to gains in effective conductivity of the order of 100–1000 %*.

5.2. Shear-Induced Monodomains at Dilute Concentrations

Our goal here is to extract the flow-induced scaling corrections to the above results, Equations 20–25, as well as the weak anisotropy induced by weak shear flow. We analyze the PDF $f(\mathbf{m})$ arising from weak steady shear of dilute spheroidal nematic polymers,[9] where the asymptotic parameter is the Peclet number *Pe*, the ratio of shear rate to average molecular relaxation rate. The normalized flow field is $\mathbf{v} \equiv Pe(y,0,0)$, where $0 < Pe \ll 1$. The result is Equation 26

$$\begin{aligned} f &= \frac{1}{\sqrt{4\pi}}(f_0 + Pef_1 + O(Pe^2)) \quad \text{with} \\ f_0 &= \frac{1}{\sqrt{4\pi}}, \quad f_1 = \frac{i}{2}\sqrt{\frac{5}{6}}\frac{a}{N-5}(Y_2^2 - Y_2^{-2}) \end{aligned} \tag{26}$$

where $a = (r^2-1)/(r^2+1)$ is the molecule geometry parameter, N is a dimensionless concentration related to θ_2 by Equation 27

$$\frac{N}{\theta_2} = \frac{8r}{\pi} \tag{27}$$

and Y_2^2 and Y_2^{-2}, are spherical harmonics which capture anisotropy of the orientational distribution of the nano-inclusions generated by the shear flow. Equation 26 is valid for $0 < N < 5\text{–}1.869a^{1/2}Pe^{1/2}$, equivalently for $0 < \theta_2 < 1/r(1.9635\text{–}0.734\sqrt{(r^2-1)/(r^2+1)}Pe^{1/2})$, the range of volume fractions for which the sheared isotropic phase persists and is stable. The upper bound on N was first derived by See, Doi, and Larson[24] and corresponds to a turning-point bifurcation of the shear-perturbed Smoluchowski equation.[9] These scaling properties are necessary to control the PDF expansion, Equation 26, and see that it is bounded at the upper limit on θ_2 (respectively, N) as the shear-perturbed, nearly isotropic steady states become unstable.

We now simply insert Equation 26 into Equation 11 and compute the integral. To first order in *Pe*, we have Equation 28

$$\mathbf{M}(f(\mathbf{m})) = \begin{pmatrix} \frac{1}{3} & -\frac{Pe}{6(N-5)} & \\ -\frac{Pe}{6(N-5)} & \frac{1}{3} & 0 \\ 0 & 0 & \frac{1}{3} \end{pmatrix} \tag{28}$$

whose principal values are given in Equations 29a–c

$$d_1 = \frac{1}{3} + \frac{Pe}{6(N-5)} \tag{29a}$$

$$d_2 = \frac{1}{3} \tag{29b}$$

$$d_3 = \frac{1}{3} - \frac{Pe}{6(N-5)} \tag{29c}$$

with principal axes, $\mathbf{n}_j$, listed below.

The anisotropic effective conductivity tensor Σ^{e} follows in explicit form from $\mathbf{M}(f)$ by Equation 12, and, more precisely, from Equations 17–19 given more refined information. The principal directions $\mathbf{n}_j$ of $\Sigma^{\mathrm{e}}_{\theta_2}$ (inherited from $\mathbf{M}$) at leading order are aligned midway between the flow (x) and flow-gradient (y) directions and along the vorticity (z) axis, Equations 30a–c

$$\mathbf{n}_1 = (1,1,0) \tag{30a}$$

$$\mathbf{n}_2 = (0,0,1) \tag{30b}$$

$$\mathbf{n}_3 = (1,-1,0) \tag{30c}$$

where the corresponding *principal values* σ_j^{e} *of* $\Sigma^{\mathrm{e}}_{\theta_2}$ *are distinct and ordered*, $\sigma_1^{\mathrm{e}} = \sigma^{\mathrm{e}}_{\max} > \sigma_2^{\mathrm{e}} = \sigma^{\mathrm{e}}_{\mathrm{vorticity}} > \sigma_3^{\mathrm{e}} = \sigma^{\mathrm{e}}_{\min}$, with explicit formulas given below.

- For $L_a/(\sigma_1/\sigma_2) \gg 1$, the three distinct principal values of $\Sigma^{\mathrm{e}}_{\theta_2}$ are given by Equations 31a–c

$$\sigma^{e}_{\max} \approx \sigma_1(1+\frac{\theta_2}{3\,L_a}) + \frac{Pe\;\theta_2\;\sigma_1}{6\,(5-N)\,L_a} \approx \sigma_1 + \sigma_1(\varepsilon^{\mathrm{iso}} + \varepsilon^{\mathrm{iso}}_{Pe}) \tag{31a}$$

$$\sigma^{e}_{\mathrm{vorticity}} \approx \sigma_1(1+\frac{\theta_2}{3\,L_a}) \approx \sigma_1 + \sigma_1\varepsilon^{\mathrm{iso}} \tag{31b}$$

$$\sigma^{e}_{\min} \approx \sigma_1(1+\frac{\theta_2}{3\,L_a}) - \frac{Pe\;\theta_2\;\sigma_1}{6\,(5-N)\,L_a} \approx \sigma_1 + \sigma_1(\varepsilon^{\mathrm{iso}} - \varepsilon^{\mathrm{iso}}_{Pe}) \tag{31c}$$

The *maximum relative conductivity enhancement* is given by Equation 32

$$\begin{aligned} \varepsilon_{\max} &= \frac{(\sum^{e}_{\theta_2,Pe} - \sum^{e}_{0,0})}{\sigma_1} : \mathbf{n}_1\mathbf{n}_1 = \frac{\sigma^{e}_{\max} - \sigma_1}{\sigma_1} \\ &= \frac{(\sum^{e}_{\theta_2,Pe} - \sum^{e}_{\theta_2,0} + \sum^{e}_{\theta_2,0} - \sum^{e}_{0,0})}{\sigma_1} : \mathbf{n}_1\mathbf{n}_1 \\ &\approx \frac{\theta_2}{3L_a} + \frac{Pe\;\theta_2}{6(5-N)L_a} \\ &\approx \varepsilon^{\mathrm{iso}} + \varepsilon^{\mathrm{iso}}_{Pe} \end{aligned} \tag{32}$$

ADVANCED FUNCTIONAL MATERIALS

- For $L_a/(\sigma_1/\sigma_2) \sim O(1)$, the three distinct principal values of $\Sigma^{e}_{\theta_2}$ and maximum relative conductivity enhancement are given by Equations 33a–d

$$\sigma^{e}_{\max} \approx \sigma_1 + \frac{\theta_2\,\sigma_2}{3\,(1+\frac{L_a}{\sigma_1/\sigma_2})} + \frac{Pe\;\theta_2\;\sigma_2}{6\,(5-N)\,(1+\frac{L_a}{\sigma_1/\sigma_2})} \approx$$

$$\sigma_1 + \sigma_1(\varepsilon^{\mathrm{iso}} + \varepsilon^{\mathrm{iso}}_{Pe}) \tag{33a}$$

$$\sigma^{e}_{\mathrm{vorticity}} \approx \sigma_1 + \frac{\theta_2\,\sigma_2}{3\,(1+\frac{L_a}{\sigma_1/\sigma_2})} \approx \sigma_1 + \sigma_1\varepsilon^{\mathrm{iso}} \tag{33b}$$

$$\sigma^{e}_{\min} \approx \sigma_1 + \frac{\theta_2\,\sigma_2}{3\,(1+\frac{L_a}{\sigma_1/\sigma_2})} - \frac{Pe\;\theta_2\;\sigma_2}{6\,(5-N)\,(1+\frac{L_a}{\sigma_1/\sigma_2})} \approx$$

$$\sigma_1 + \sigma_1(\varepsilon^{\mathrm{iso}} - \varepsilon^{\mathrm{iso}}_{Pe}) \tag{33c}$$

$$\varepsilon_{\max} \approx \frac{\theta_2\,(\sigma_2/\sigma_1)}{3\,(1+\frac{L_a}{\sigma_1/\sigma_2})} + \frac{Pe\,\theta_2\,(\sigma_2/\sigma_1)}{6(5-N)\,(1+\frac{L_a}{\sigma_1/\sigma_2})} \approx \varepsilon^{\mathrm{iso}} + \varepsilon^{\mathrm{iso}}_{Pe} \tag{33d}$$

- For $L_a/(\sigma_1/\sigma_2) \ll 1$, we have Equations 34a–d

$$\sigma^{e}_{\max} \approx \sigma_1(1 + \frac{\theta_2\sigma_2}{3\sigma_1}) + \frac{Pe\;\theta_2\;\sigma_2}{6\,(5-N)} \approx \sigma_1 + \sigma_1(\varepsilon^{\mathrm{iso}} + \varepsilon^{\mathrm{iso}}_{Pe}) \tag{34a}$$

$$\sigma^{e}_{\mathrm{vorticity}} \approx \sigma_1(1 + \frac{\theta_2\sigma_2}{3\sigma_1}) \qquad \approx \sigma_1 + \sigma_1\varepsilon^{\mathrm{iso}} \tag{34b}$$

$$\sigma^{e}_{\min} \approx \sigma_1(1 + \frac{\theta_2\sigma_2}{3\sigma_1}) - \frac{Pe\;\theta_2\;\sigma_2}{6\,(5-N)} \approx \sigma_1 + \sigma_1(\varepsilon^{\mathrm{iso}} - \varepsilon^{\mathrm{iso}}_{Pe}) \tag{34c}$$

$$\varepsilon_{\max} \approx \frac{\theta_2\,(\sigma_2/\sigma_1)}{3} + \frac{Pe\,\theta_2\,(\sigma_2/\sigma_1)}{6\,(5-N)} \approx \varepsilon^{\mathrm{iso}} + \varepsilon^{\mathrm{iso}}_{Pe} \tag{34d}$$

Note: In all three limits, the overall conductivity enhancement is a sum of the quiescent isotropic enhancement $\varepsilon^{\mathrm{iso}}$ and a flow-induced enhancement $\varepsilon^{\mathrm{iso}}_{Pe}$.

The relative size of $\varepsilon^{\mathrm{iso}}$ and $\varepsilon^{\mathrm{iso}}_{Pe}$ defers to 1/3 versus $Pe/(6(5–N))$. The latter term increases with both Pe and N, and is bounded from above by $O(Pe^{1/2})$. The contributions appear to be comparable even at weak shear rates, so Equation 12 predicts a definite benefit from weak flow processing.

We can also define the conductivity analog of optical birefringence Bi, which is given by Equation 35

$$Bi = d_{\max} - d_{\min} = d_1 - d_3 \tag{35}$$

where d_i are the principal values of $\mathbf{M}(f(\mathbf{m}))$. The analog is the *maximum conductivity contrast* along the major and minor principal axes, $\sigma^{e}_{\mathrm{contrast}}$, given by Equation 36

$$\sigma^{e}_{contrast} = \sigma_1(\varepsilon_{\max} - \varepsilon_{\min}) \tag{36}$$

Naturally, *the maximum anisotropy in conductivity comes purely from the shear flow* for these three dilute concentration cases, Equation 37

$$\varepsilon_{\max} - \varepsilon_{\min} \approx \begin{cases} \dfrac{Pe\,\theta_2}{3\,(5-N)\,L_a}, & \dfrac{L_a}{\sigma_1/\sigma_2} \gg 1 \\ \dfrac{Pe\,\theta_2\,(\sigma_2/\sigma_1)}{3\,(1+\frac{L_a}{\sigma_1/\sigma_2})\,(5-N)}, & \dfrac{L_a}{\sigma_1/\sigma_2} \sim O(1) \\ \dfrac{Pe\,\theta_2\,(\sigma_2/\sigma_1)}{3\,(5-N)}, & \dfrac{L_a}{\sigma_1/\sigma_2} \ll 1 \end{cases} \tag{37}$$

Note: Indeed, the above expressions can be directly cast in terms of the optical birefringence parameter, Bi, by using the formulas for d_j in Equation 29. By doing so, we find Equation 38

$$\sigma^{e}_{contrast} = \sigma_1(\varepsilon_{\max} - \varepsilon_{\min}) \approx$$

$$\begin{cases} \dfrac{\sigma_1\theta_2}{L_a}Bi, & \dfrac{L_a}{\sigma_1/\sigma_2} \gg 1 \\ \dfrac{\theta_2\,\sigma_2}{(1+\frac{L_a}{\sigma_1/\sigma_2})}Bi, & \dfrac{L_a}{\sigma_1/\sigma_2} \sim O(1) \\ \theta_2\,\sigma_2\,Bi, & \dfrac{L_a}{\sigma_1/\sigma_2} \ll 1 \end{cases} \tag{38}$$

5.3. Quiescent Nematic Phases and Mesoscopic Approximations

Exact formulas for the PDF $f(\mathbf{m})$ at nematic concentrations do not exist, except in the limit as $N \to \infty$.[19] Alternatively, we employ second-moment closure models, where scaling properties can be derived and subsequently compared with numerical computations or with other closures. We consider the Doi closure model for illustrative purposes, given in terms of the orientation tensor $\mathbf{Q}$, $\mathbf{Q} = \mathbf{M}–1/3\mathbf{I}$, capturing the deviatoric part of $\mathbf{M}(f)$ which measures the departure from isotropy. Nematic states exist for sufficiently high concentration $N > 8/3$, equivalently for $\theta_2 > \pi/(3r)$, in the Doi closure model. (We remark that N has been effectively scaled by the closure; $N = 8/3$ here is only proportional to the critical value for kinetic theory, which for $r \to \infty$ is approximately $N = 4$.) For the uniaxial nanoinclusion distribution at rest, $\mathbf{Q} = s(\mathbf{nn}–\mathbf{I}/3)$, where s is the uniaxial order parameter ($s = d_1–d_2, d_2 = d_3$), which measures the anisotropy of the distribution; the isotropic phase has $s = 0$, whereas for the stable nematic phase, s is given by Equation 39

$$s = \frac{1}{4}\left(1 + 3\sqrt{1 - \frac{8}{3N}}\right) \in \left(\frac{1}{4}, 1\right) \tag{39}$$

The uniaxial director $\mathbf{n} = (\cos\phi\sin\theta, \sin\phi\sin\theta, \cos\theta)$ is the principal axis of $\mathbf{Q}$ or $\mathbf{M}$ corresponding to the distinct, maximum eigenvalue (d_1 of $\mathbf{M}$, d_1–1/3 of $\mathbf{Q}$).

Consider the orientation tensor $\mathbf{Q}$ at rest, corresponding to major director $\mathbf{n}_0 = (\cos\phi_0\sin\theta_0, \sin\phi_0\sin\theta_0, \cos\theta_0)$. The nematic phase is $O(3)$ degenerate, meaning any similarity transformation of $\mathbf{Q}$, $\mathcal{O}^t\mathbf{Q}\mathcal{O}$, is also an equilibrium, where $\mathcal{O}\in O(3)$, the orthogonal group. From the primary formula, Equation 12, and the remarks below, the principal axes of the effective conductivity tensor $\Sigma^e_{\theta_2}$ are also $O(3)$ invariant, whereas, the anisotropic principal values σ_i^e for $\Sigma^e_{\theta_2}$ have scaling behavior that depends on the three limiting cases of L_a versus σ_1/σ_2

- For $L_a/(\sigma_1/\sigma_2) \gg 1$

$$\sigma_1^e = \sigma^e_{\max} \approx \sigma_1 + \frac{\theta_2\,\sigma_1}{3\,L_a}(1+2s)$$

$$\sigma_2^e = \sigma_3^e = \sigma^e_{\min} \approx \sigma_1 + \frac{\theta_2\,\sigma_1}{3\,L_a}(1-s)$$

$$\varepsilon_{\max} \approx \frac{\theta_2}{3\,L_a} + \frac{2\,s\,\theta_2}{3\,L_a} \approx \varepsilon^{\text{iso}} + \varepsilon^{\text{nema}} \tag{40}$$

- For $L_a/(\sigma_1/\sigma_2) \sim O(1)$

$$\sigma_1^e = \sigma^e_{\max} \approx \sigma_1 + \frac{\theta_2\,\sigma_2}{3\,(1+\dfrac{L_a}{\sigma_1/\sigma_2})}(1+2s)$$

$$\sigma_2^e = \sigma_3^e = \sigma^e_{\min} \approx \sigma_1 + \frac{\theta_2\,\sigma_2}{3\,(1+\dfrac{L_a}{\sigma_1/\sigma_2})}(1-s)$$

$$\varepsilon_{\max} \approx \frac{\theta_2\,(\sigma_2/\sigma_1)}{3\,(1+\dfrac{L_a}{\sigma_1/\sigma_2})} + \frac{2\,s\,\theta_2\,(\sigma_2/\sigma_1)}{3\,(1+\dfrac{L_a}{\sigma_1/\sigma_2})} \approx \varepsilon^{\text{iso}} + \varepsilon^{\text{nema}} \tag{41}$$

- For $L_a/(\sigma_1/\sigma_2) \ll 1$

$$\sigma_1^e = \sigma^e_{\max} \approx \sigma_1 + \frac{1}{3}\theta_2\sigma_2(1+2s)$$

$$\sigma_2^e = \sigma_3^e = \sigma^e_{\min} \approx \sigma_1 + \frac{1}{3}\theta_2\sigma_2(1-s)$$

$$\varepsilon_{\max} \approx \frac{\theta_2\,(\sigma_2/\sigma_1)}{3} + \frac{2\,\theta_2\,(\sigma_2/\sigma_1)\,s}{3} \approx \varepsilon^{\text{iso}} + \varepsilon^{\text{nema}} \tag{42}$$

The maximum anisotropy in conductivity of the quiescent nematic phase for these three cases is now explicit, Equation 43

$$\varepsilon_{\max} - \varepsilon_{\min} \approx \begin{cases} \dfrac{\theta_2 s}{L_a}, & \dfrac{L_a}{\sigma_1/\sigma_2} \gg 1 \\ \dfrac{\theta_2(\sigma_2/\sigma_1)s}{1+\dfrac{L_a}{\sigma_1/\sigma_2}}, & \dfrac{L_a}{\sigma_1/\sigma_2} \sim O(1) \\ \dfrac{\theta_2\sigma_2 s}{\sigma_1}, & \dfrac{L_a}{\sigma_1/\sigma_2} \ll 1 \end{cases} \tag{43}$$

Comparison of these scaling properties, Equation 43 of the pure nematic phase with both the pure isotropic phase (Sect. 5.1) and the shear-induced isotropic phase (Sect. 5.2) reveals the same isotropic enhancement $\varepsilon^{\text{iso}\circ}$ *plus* a magnification of the anisotropic enhancement, Equation 37, with the asymptotic pre-factor Pe replaced by the $O(1)$ scalar order parameter $s\in(1/4,1)$. As we illustrate later, these scaling properties clearly expose the dominant effect of nematic order on the conductivity enhancement, with a discontinuous gain in $\varepsilon_{\max}$ as the order parameter S jumps at the disorder–order phase transition ($N = 8/3$ in this model).

5.4. Shear-Perturbed, Flow-Aligned Monodomains at Nematic Concentrations

To this point, we have characterized the effects of shear on the isotropic phase and of the order transition to the nematic phase, to which we now couple the effects due to weak shear. This will only perturbatively alter the principal values of the anisotropic conductivity tensor, but has the important effect of selecting the principal axes of anisotropy, that is, breaking the $O(3)$ degeneracy of the nematic phase. The perturbed solution $\mathbf{Q}$ corresponding to a shear-induced monodomain at low shear rate ($Pe \ll 1$) is explicitly constructed, Equation 44[11]

$$\mathbf{Q} = s(\mathbf{nn} - \frac{1}{3}\mathbf{I}) + Pe\left[\frac{c_1}{2}\begin{pmatrix}0&1&0\\1&0&0\\0&0&0\end{pmatrix} + c_2\begin{pmatrix}1&0&0\\0&1&0\\0&0&-2\end{pmatrix} + c_3\begin{pmatrix}1&0&0\\0&-1&0\\0&0&0\end{pmatrix}\right] + O(Pe^2) \tag{44}$$

where s depends only on θ_2 from Equation 39, the $O(1)$ estimate of the shear-selected major director of $\mathbf{Q}$ is $\mathbf{n} = (\cos\phi_L, \sin\phi_L, 0)$, where the so-called Leslie alignment angle

$$\varphi_L = \frac{1}{2}\cos^{-1}\left(\frac{3\,s}{a\,(2+s)}\right)$$

depends on θ_2 (through s) and aspect ratio (through a); and the constants c_i depend on θ_2 and r, Equation 45a–c

$$c_1 = \frac{(1-s)^2(1+2s)}{9s(4s-1)}\left[a\,(11s+4) - \frac{9s^2(19s+8)}{a\,(2+s)^2}\right] \tag{45a}$$

$$c_2 = \frac{(1-s)^2(1+2s)\tan 2\varphi_L}{6\,(4s-1)} \tag{45b}$$

$$c_3 = \frac{3s(1-s)^2(1+2s)(19s+8)\tan 2\varphi_L}{6\,a\,(2+s)^2(4s-1)} \tag{45c}$$

The $O(Pe)$ shear-dependent angle $\tilde{\phi}_L$ of the major director $\tilde{\mathbf{n}}$ of $\mathbf{Q}$, $\tilde{\mathbf{n}} = (\cos\tilde{\phi}_L, \sin\tilde{\phi}_L, 0)$, is given by Equation 46

$$\cos 2\tilde{\phi} = \cos 2\varphi_L + Pe\frac{4(1-s)^2(1+2s)^2\sin 2\varphi_L}{3s(2+s)(4s-1)} + O(Pe^2) \tag{46}$$

The principal values of $\Sigma^e_{\theta_2}$ in the three different limiting cases follow, where $\sigma^e_{\max}$ is associated with the principal axis, $\tilde{\mathbf{n}}$,

$\sigma^{e}_{\text{vorticity}}$ with (0,0,1), and $\sigma^{e}_{\min}$ with the normal $\tilde{\mathbf{n}}^{\perp}$ to $\tilde{\mathbf{n}}$ in the shear plane. This implies, for example, that the maximum conductivity anisotropy lies in the plane of flow deformation for these flow-aligned monodomains. (As the shear rate and volume fraction vary, a remarkable array of transient orientational distributions emerges,[8,10,13–15] whose conductivity will likewise oscillate until the system is quenched. These dynamic properties will be reported in a subsequent study.)

- For $L_a/(\sigma_1/\sigma_2) \gg 1$,

$$\sigma^{e}_{\max} \approx \sigma_1 + \frac{\theta_2\sigma_1}{3\,L_a}\left(1 + 2s + \chi(a,\theta_2)Pe\right) \tag{47a}$$

$$\sigma^{e}_{\text{vorticity}} \approx \sigma_1 + \frac{\theta_2\sigma_1}{3\,L_a}\left(1 - s - \chi(a,\theta_2)Pe\frac{s+2}{3(1+2s)}\right) \tag{47b}$$

$$\sigma^{e}_{\min} \approx \sigma_1 + \frac{\theta_2\sigma_1}{3\,L_a}\left(1 - s - \chi(a,\theta_2)Pe\frac{5s+1}{3(1+2s)}\right) \tag{47c}$$

where χ is a recurring factor that depends only on the aspect ratio parameter a and the volume fraction θ_2, depicted in Figure 3 for aspect ratio r=100, Equation 48

$$\chi(a,\theta_2) = \frac{a\,(1-s)^2\,(1+2s)^2\,\sin 2\varphi_L}{s\,(4s-1)} \tag{48}$$

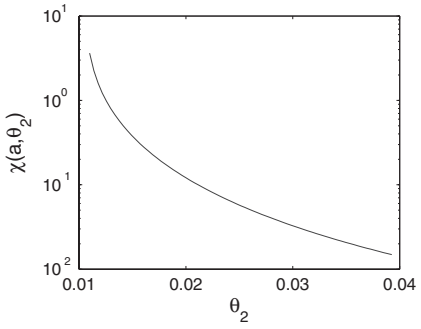

Figure 3. The scaling factor $\chi(a,\theta_2)$ versus θ_2, for r=100.

The maximum enhancement is given by Equations 49a and b

$$\varepsilon_{\max} \approx \frac{\theta_2}{3\,L_a}\left(1 + 2s + \chi(a,\theta_2)Pe\right) \approx \varepsilon^{\text{iso}} + \varepsilon^{\text{nema}} + \varepsilon^{\text{nema}}_{Pe} \tag{49a}$$

$$\varepsilon^{\text{nema}}_{Pe} \approx Pe \cdot \frac{\theta_2}{3\,L_a} \cdot \chi(a,\theta_2) \tag{49b}$$

where the first two terms are precisely the result, Equation 40, without flow, and the new term is the flow-induced enhancement $\varepsilon^{\text{nema}}_{Pe}$ of the nematic phase. We note that even though Pe is small, for example, $Pe \sim 0.1$, the product $\chi \cdot Pe$ is comparable to the other two factors 1 and 2s, when θ_2 is close to 1 %.

The decomposition formula, Equation 49a will be reproduced in the two remaining regimes, where the precise forms of the isotropic (dilute) enhancement ε^{iso}, the boost $\varepsilon^{\text{nema}}$ from the nematic phase, and the flow-induced enhancement of the nematic phase $\varepsilon^{\text{nema}}_{Pe}$, depend on the ratio of L_a and σ_1/σ_2. In all cases, the property enhancement decomposes into the sum of these three contributions, illustrated in Section 6.

- For $L_a/(\sigma_1/\sigma_2) \sim O(1)$,

$$\sigma^{e}_{\max} \approx \sigma_1 + \frac{\theta_2\sigma_2}{3\,(1+\frac{L_a}{\sigma_1/\sigma_2})}\left(1 + 2s + \chi(a,\theta_2)Pe\right) \tag{50a}$$

$$\sigma^{e}_{\text{vorticity}} \approx \sigma_1 + \frac{\theta_2\sigma_2}{3\,(1+\frac{L_a}{\sigma_1/\sigma_2})}\left(1 - s - \chi(a,\theta_2)Pe\frac{s+2}{3(1+2s)}\right) \tag{50b}$$

$$\sigma^{e}_{\min} \approx \sigma_1 + \frac{\theta_2\sigma_2}{3\,(1+\frac{L_a}{\sigma_1/\sigma_2})}\left(1 - s - \chi(a,\theta_2)Pe\frac{5s+1}{3(1+2s)}\right) \tag{50c}$$

$$\varepsilon_{\max} \approx \frac{\theta_2\,(\sigma_2/\sigma_1)}{3\,(1+\frac{L_a}{\sigma_1/\sigma_2})}\left(1 + 2s + \chi(a,\theta_2)Pe\right) \approx \varepsilon^{\text{iso}} + \varepsilon^{\text{nema}} + \varepsilon^{\text{nema}}_{Pe} \quad \text{where} \tag{50d}$$

$$\varepsilon^{\text{nema}}_{Pe} \approx Pe \cdot \frac{\theta_2(\sigma_2/\sigma_1)}{3(1+\frac{L_a}{\sigma_2/\sigma_1})} \cdot \chi(a,\theta_2) \tag{51}$$

- For $L_a/(\sigma_1/\sigma_2) \ll 1$,

$$\sigma^{e}_{\max} \approx \sigma_1 + \frac{\theta_2\sigma_2}{3}\left(1 + 2s + \chi(a,\theta_2)Pe\right) \tag{52a}$$

$$\sigma^{e}_{\text{vorticity}} \approx \sigma_1 + \frac{\theta_2\sigma_2}{3}\left(1 - s - \chi(a,\theta_2)Pe\frac{s+2}{3(1+2s)}\right) \tag{52b}$$

$$\sigma^{e}_{\min} \approx \sigma_1 + \frac{\theta_2\sigma_2}{3}\left(1 - s - \chi(a,\theta_2)Pe\frac{5s+1}{3(1+2s)}\right) \tag{52c}$$

$$\varepsilon_{\max} \approx \frac{\theta_2\sigma_2}{3\sigma_1}\left(1 + 2s + \chi(a,\theta_2)Pe\right) \approx \varepsilon^{\text{iso}} + \varepsilon^{\text{nema}} + \varepsilon^{\text{nema}}_{Pe} \tag{52d}$$

where

$$\varepsilon^{\text{nema}}_{Pe} \approx Pe \cdot \frac{\theta_2(\sigma_2/\sigma_1)}{3} \cdot \chi(a,\theta_2) \tag{53}$$

Finally, the maximum anisotropy in effective conductivity for these three cases is given by Equation 54

$$\varepsilon_{\max} - \varepsilon_{\min} \approx \begin{cases} \dfrac{\theta_2}{L_a}\left(s + \chi(a,\theta_2)Pe\dfrac{11s+4}{9(1+2s)}\right), & \dfrac{L_a}{\sigma_1/\sigma_2} \gg 1 \\ \dfrac{\theta_2\,(\sigma_2/\sigma_1)}{(1+\frac{L_a}{\sigma_1/\sigma_2})}\left(s + \chi(a,\theta_2)Pe\dfrac{11s+4}{9(1+2s)}\right), & \dfrac{L_a}{\sigma_1/\sigma_2} \sim O(1) \\ \theta_2\,(\sigma_2/\sigma_1)\left(s + \chi(a,\theta_2)Pe\dfrac{11s+4}{9(1+2s)}\right), & \dfrac{L_a}{\sigma_1/\sigma_2} \ll 1 \end{cases} \tag{54}$$

6. Illustrations

The scaling properties derived above will now be illustrated by graphs of the maximum relative conductivity enhancement (ε_{max}) versus volume fraction of the nanocomposite, Figures 4,5. The graphs are based on the general formula, Equation 12, and the scaling properties are validated against them. We present the properties of the composite in a hierarchy suggested by the decomposition scaling formulas, Equations 49,50,52, first (Fig. 4) amplifying the transference of the classical I–N phase transition into electrical conductivity principal values, and then (Figs. 5,6) comparing the additional enhancement due to weak shear flow.

We will use polymer–CNT composites as a model example, system (ii) below, where the polymer matrix is typically non-conductive ($\sigma_1 \sim O(10^{-8})$ $(\Omega\,\mathrm{cm})^{-1}$), and the CNTs are extremely conductive ($\sigma_2 \sim O(10^{4})$ $(\Omega\,\mathrm{cm})^{-1}$)). In these model systems, $\sigma_1/\sigma_2 \sim O(10^{-12})$, whereas the typical aspect ratio of CNTs is $r = (10^4 \sim 10^5\ \mathrm{nm})/(1 \sim 50\ \mathrm{nm}) \sim O(2\times10^2\text{–}10^5)$. From Equation 15, the geometry parameter L_a is then estimated as $L_a \sim O(10^{-4}\text{–}10^{-9})$. These estimates imply polymer–CNT composites always lie in the regime $L_a/(\sigma_1/\sigma_2) \gg 1$, that is, case 1, in all estimates of Section 5. We will illustrate the results of Equation 12 for two model systems: i) $r = 100$, $\sigma_1/\sigma_2 = 10^{-5}$; ii) $r = 1000$, $\sigma_1/\sigma_2 = 10^{-10}$. System (i) is posited to compare enhancements when the aspect ratio and contrast are less extreme, yet still significant.

Figure 4 conveys that for quiescent phases, ε_{max} inherits hysteresis, bi-stability, and discontinuous jumps between the volume fractions θ_2* where the nematic phase begins and θ_2** where the isotropic phase becomes unstable. The predictions then fall into three intervals of volume fraction: $\theta_2 < \theta_2$*; θ_2* $< \theta_2 <$ θ_2**, and $\theta_2 > \theta_2$**. For model system (i), θ_2* = 1.05 %, θ_2** = 1.18 %; for model system (ii), θ_2* = 0.105 %, θ_2** = 0.118 %.

For model system (i), the maximum enhancement ε_{max} grows over interval 1 to 792 % at θ_2*, it likewise grows over interval 3 from 1788 % at θ_2** to 3700 % at 2 % volume fraction. In the bi-stable isotropic and nematic interval, θ_2* $< \theta_2 <$ θ_2**, the isotropic phase enhancement grows from 792 to 895 %, whereas the nematic phase enhancement begins 1189 at and increases to 1788 %. Note the difference in ε_{max} between the bi-stable phases is significant: ε^{nema}_{max}–ε^{iso}_{max} is 397 % at θ_2* and grows to 893 % at θ_2**.

For model system (ii), the maximum enhancement ε_{max} grows over interval 1 to 5274 % at θ_2*, it likewise grows over interval 3 from 11 900 % at θ_2** to 25 000 % at 0.2 % volume fraction. In the bi-stable isotropic and nematic interval θ_2* $< \theta_2 <$ θ_2**, the isotropic phase enhancement grows from 5274 % to 5953 %, whereas the nematic phase enhancement begins at 7924 % and increases to 11 900 %. Note the difference ε^{nema}_{max}–ε^{iso}_{max} between the bi-stable phases is 2650 % at θ_2* and grows to 6000 % at θ_2**.

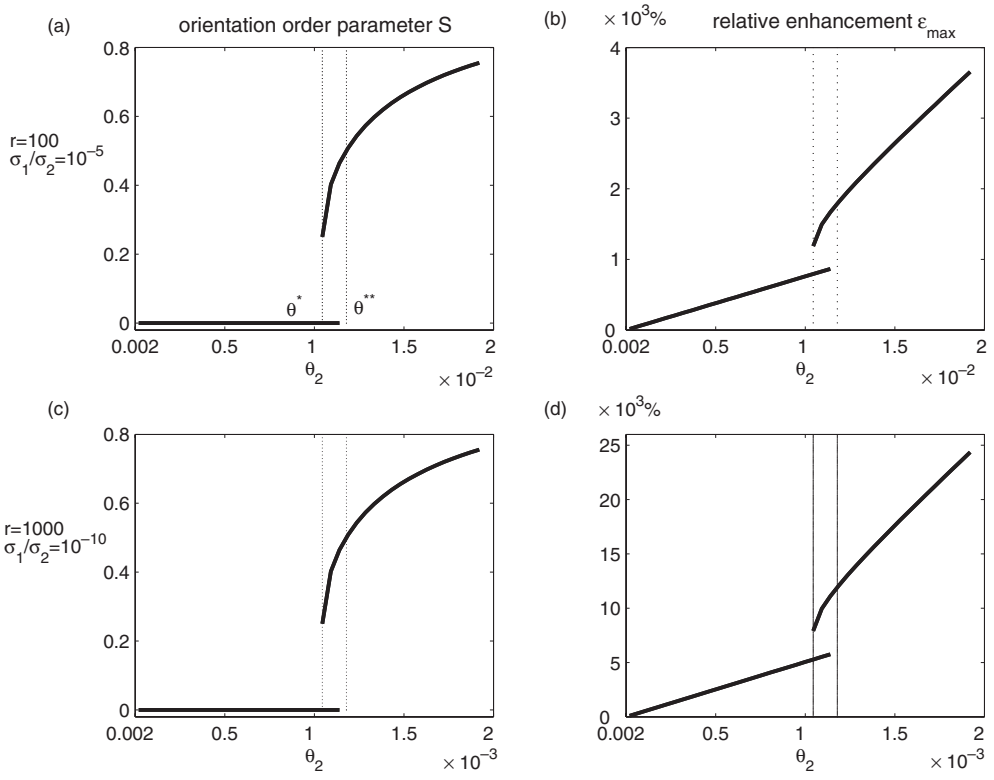

Figure 4. Quiescent orientation–conductivity enhancement correlations versus volume fraction for two model nanocomposites. Hysteresis associated with the quiescent I–N phase transition is duplicated in the effective conductivity property enhancement for two model systems. a,c) Order parameter *S* versus volume fraction θ_2. b,d) Corresponding relative conductivity enhancement ε_{max}. Model-system aspect ratio and conductivity contrasts are indicated. The two vertical lines mark the critical concentration, θ_2* and θ_2**, of each model system; θ_2* is the onset of the nematic phase; θ_2** is the instability transition of the isotropic phase.

ADVANCED FUNCTIONAL MATERIALS

Figure 5 shows that at the weak normalized shear rate $Pe = 0.1$, the hysteresis cycle has been pulled out, leaving a unique stable equilibrium phase for each volume fraction θ_2. (The volume-fraction interval 2 above, of the bi-stable phases, is gone.) The corresponding $\varepsilon_{\max}$ for each equilibrium phase mirrors the monotonicity of the scalar order parameter *S*.

Figure 6 isolates the flow-induced contribution to $\varepsilon_{\max}$ for systems (i) and (ii): Figures 6a,c, respectively. Figures 6a,c show that the flow-induced contribution $\varepsilon_{Pe}^{\text{iso}}$ on the isotropic branch grows rapidly, whereas $\varepsilon_{Pe}^{\text{nema}}$, the nematic flow-induced contribution, is greatest at the onset of the nematic phase, $\theta_2 = \theta_2{}^*$, and then rapidly falls off to negligible gain. Figures 6b,d provide the fraction $\varepsilon_{Pe}^{\text{iso}}/\varepsilon_{\max}$ and $\varepsilon_{Pe}^{\text{nema}}/\varepsilon_{\max}$ of the conductivity enhancement due specifically to the flow contribution. The figures are almost identical for systems (i) and (ii), after accounting for the volume-fraction scaling due to *r*. On the isotropic branch, the flow contribution ranges from 10 to 53 %, whereas on the nematic branch, the range is 23 % down to almost zero. These figures underscore the fact that the gain due to flow has a peak, which suggests flow-induced gain can be optimized if these scaling features persist into more general processing regimes.

7. Conclusion

We have derived $\sum_{\theta_2}^{e}$, the effective electrical conductivity tensor, in explicit form for nanocomposites with volume fraction θ_2 of nematic polymers with matrix conductivity σ_1 and nano-inclusion conductivity σ_2. This result is based on volume averaging over an arbitrary orientational probability distribution of monodisperse, spheroidal molecular inclusions. The formula encodes both quiescent and weak shear bulk phases through the second moment tensor of the orientational PDF; all higher moments of the PDF are rigorously shown to not enter $\sum_{\theta_2}^{e}$ at leading order in θ_2.

We then infer an explicit decomposition of the *conductivity enhancement* ε (associated with the maximum principal value of $\sum_{\theta_2}^{e}$) into contributions ε^{iso} of the isotropic phase, $\varepsilon^{\text{nema}}$ of the nematic phase, and ε_{Pe} of the shear-induced isotropic or nematic phase, Equation 55

$$\varepsilon = \varepsilon^{\text{iso}} + \varepsilon^{\text{nema}} + \varepsilon_{Pe} \tag{55}$$

The directions and degrees of anisotropy are also characterized. Refined scaling laws are then determined depending on the relative size of two independent large parameters in nematic polymer nanocomposites, the molecular aspect ratio *r* and the conductivity contrast σ_2/σ_1.

Key features of the analysis are:

- The conductivity enhancement inherits the hysteresis of the isotropic–nematic phase diagram. That is, $\varepsilon^{\text{nema}}$ is a dominant contribution that emerges spontaneously at the critical volume fraction $\theta_2 = \theta_2{}^*$ of the I–N transition. The analogy with a percolation threshold is compelling, and will be addressed elsewhere.

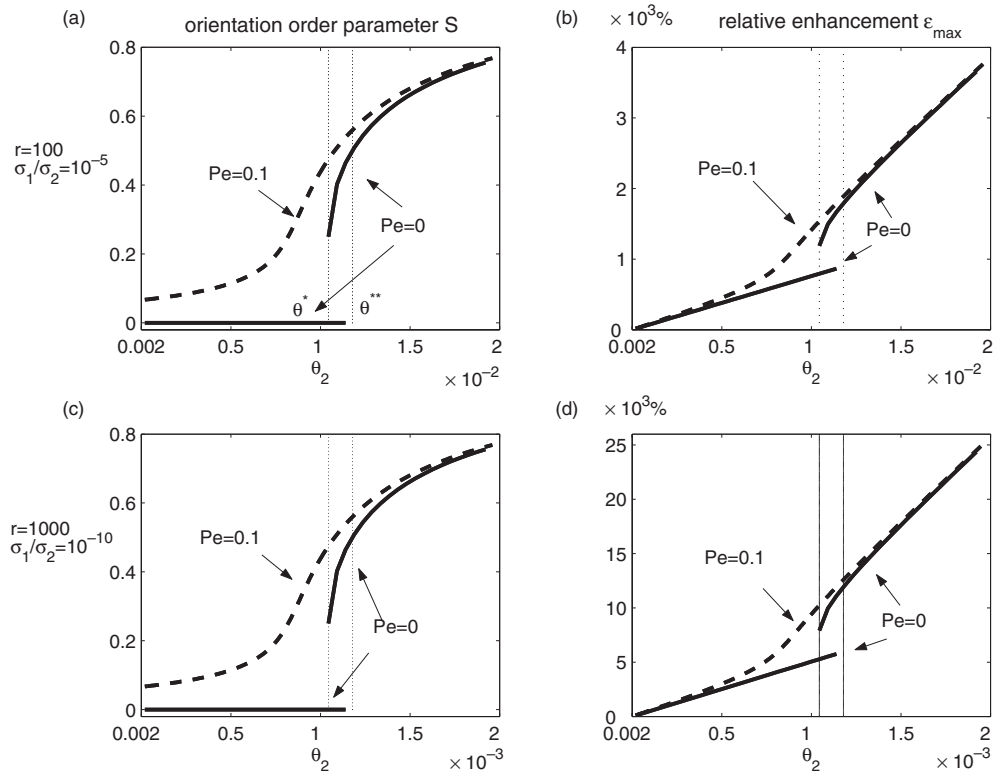

Figure 5. Comparison between shear-induced and quiescent orientation order parameter versus volume fraction, and the corresponding effective conductivity enhancements for the two model systems of Figure 5. a,c) Order parameter *S* versus volume fraction θ_2. b,d) Corresponding relative conductivity enhancements.

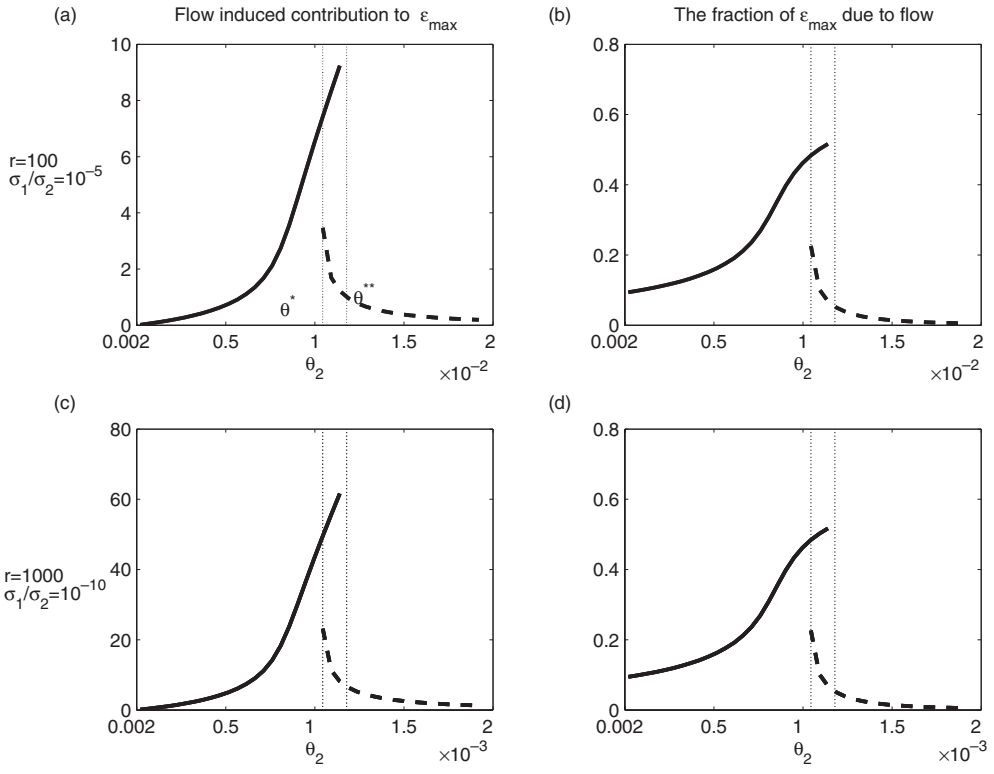

Figure 6. a,c) The flow-induced contribution to ε_{max}, defined by $\varepsilon_{max}^{Pe=0}$, where $\varepsilon_{max}^{Pe=0}$ depends on the volume fraction (Fig. 5). In the bi-stable region, we show the flow contribution for both stable phases at $Pe=0$. b,d) The fraction of the total enhancement, ε_{max}, contributed by the flow-induced values ε_{Pe}^{iso}, ε_{Pe}^{nema} respectively.

- The high conductivity contrast $\sigma_2/\sigma_1 \gg 1$ and high molecule aspect ratio $r \gg 1$ are sufficient to overwhelm the low volume fraction $\theta_2 \ll 1$. For typical CNT composites, we predict conductivity enhancements of the order of 1000–10 000 %. These extreme gains are greater than those reported in experimental systems, compelling the incorporation of additional effects as noted below.
- The principal axes of $\Sigma_{\theta_2}^{e}$ follow those of the second moment **M** of the nano-inclusion orientational distribution function $f(\mathbf{m})$, a rigorous consequence of our main formula, Equation 12, which is intuitively natural.
- These results for bulk homogenous mesophases of nematic polymer nanocomposites lay the groundwork for extensions to heterogeneity, (i.e., ensembles of local mesophases with confinement and flow-induced spatial structures), more general flow rates and flow type, and the incorporation of effects of the "interphase" between the matrix and nano-inclusions.

Received: May 12, 2004
Final version: August 11, 2004

[1] R. A. Vaia, *Polymer Nanocomposites*, Oxford University Press, London **2002**.
[2] R. H. Lusti, P. J. Hine, A. A. Gusev, *Compos. Sci. Technol.* **2002**, *62*, 1927.
[3] W. R. Burghardt, *Macromol. Chem. Phys.* **1998**, *199*, 471.
[4] M. Doi, *J. Polym. Sci., Part B: Polym. Phys.* **1981**, *19*, 229.
[5] M. Doi, S. F. Edwards, *The Theory of Polymer Dynamics*, Oxford University Press, London **1986**.
[6] S. Hess, *Z. Naturforsch.* **1976**, *31a*, 1034.
[7] M. Kroger, *Phys. Rep.* **2004**, *390*, 453.
[8] V. Faraoni, M. Grosso, S. Crescitelli, P. L. Maffettone, *J. Rheol.* **1999**, *43*, 829.
[9] M. G. Forest, R. Zhou, Q. Wang, *J. Non-Newton. Fluid Mech.* **2004**, *116*, 183.
[10] R. G. Larson, H. Ottinger, *Macromolecules* **1991**, *24*, 6270.
[11] M. G. Forest, R. Zhou, Q. Wang, *J. Rheol.* **2003**, *47*, 105.
[12] M. G. Forest, Q. Wang, R. Zhou, E. Choate, *J. Non-Newton. Fluid Mech.* **2004**, *118*, 17.
[13] M. G. Forest, Q. Wang, R. Zhou, *Rheol. Acta* **2004**, *43*, 17.
[14] M. G. Forest, Q. Wang, R. Zhou, *Rheol. Acta* **2005**, *44*, 80.
[15] M. Grosso, R. Keunings, S. Crescitelli, P. L. Maffettone, *Phys. Rev. Lett.* **2001**, *86*, 3184.
[16] M. G. Forest, Q. Wang, H. Zhou, R. Zhou, *J. Rheol.* **2004**, *48*, 175.
[17] G. W. Milton, *The Theory of Composites*, Cambridge University Press, Cambridge, UK **2002**.
[18] J. A. Stratton, *Electromagnetic Theory*, McGraw-Hill Company, New York **1941**.
[19] R. Constantin, P. I. Kevrekidis, E. S. Titi, University of Chicago preprint **2004**.
[20] A. N. Beris, B. J. Edwards, *Thermodynamics of Flowing Systems with Internal Microstructure*, Oxford University Press, London **1994**.
[21] P. G. de Gennes, J. Prost, *The Physics of Liquid Crystals*, Oxford University Press, London **1993**.
[22] R. G. Larson, *The Structure and Rheology of Complex Fluids*, Oxford University Press, London **1993**.
[23] M. G. Forest, Q. Wang, *Rheol. Acta* **2003**, *42*, 20.
[24] H. See, M. Doi, R. G. Larson, *J. Chem. Phys.* **1990**, *92*, 792.

